# Bragg Diffraction Patterns as Graph Characteristics

Francisco Escolano and Edwin R. Hancock

Department of Computer Science and AI,
University of Alicante, 03690, Alicante Spain
sco@dccia.ua.es
Department of Computer Science,
University of York, York, YO10 5GH, UK
erh@cs.york.ac.uk

**Abstract.** In this paper we establish a link between diffraction theory and graph characterization through the Schrödinger operator. This provides a natural way of characterizing wave propagation on a graph. In order to do so, we compute the spatio-temporal Fourier transform of the operator and then pack its spherical representation in a point of a Stiefel manifold. We show that when the temporal interval of analysis is set according to quantum efficiency principles the proposed approach outperforms the alternatives in graph discrimination.

**Keywords:** Diffraction, Schrödinger operator, Stiefel manifolds.

## 1 Introduction

Graph characterization aims to provide a succinct way of representing graph structure that can be used distinguish or compare different types of graph, without applying graph or subgraph isomorphism (procedures that are known to be NP-complete). Popular and effective methods include random walks [1], the Ihara zeta function [2] and the spectral radius [3].

Of particular interest to us here is recent work based around the analysis of the heat kernel of a graph. The heat kernel is the solution of the heat equation on a graph, with the Laplacian matrix playing the role of conductivity matrix, i.e. controlling the flow of heat along edges with time. If the eigenvalues and eigenvectors of the Laplacian are known, then the heat kernel can be found by exponentiating the Laplacian eigensystem with time. The heat kernel determines the time evolution of a continuous time random walk on a graph, and this leads to several possible characterizations or signatures for graphs. Bai and Hancock [6] show that the moments of the heat kernel trace (i.e. its Mellin transform) are linked to the Riemann zeta function. Sun, Ovsjanikov and Guibas [11] histogram the elements of the heat kernel trace to compute the heat kernel signature, and use this for shape recognition. In a recent paper, Escolano *et al.* [4] introduced an alternative technique based on the analysis of the heat flow on a graph. Heat flow is derived from the heat kernel, which is the solution of the heat diffusion

equation. It provides a method to represent the heat transfer between the nodes of a graph over time.

Closely related to this work on the heat kernel is the wave kernel signature (WKS) [7]. This involves histogramming the elements of the wave kernel, which is the solution of the complex wave equation or Schrödinger equation associated with the graph's Laplacian matrix. While the heat equation describes how heat is transferred in a system, the Schrödinger equation characterizes the dynamics of a particle in a quantum system. In fact, the continuous time quantum walk on a graph is the solution to the Schrödinger equation, with the normalised Laplacian playing the role of a Hamiltonian. In this setting, the quantum nature of the Schrödinger equation and its complex-valued solutions give rise to many interesting non-classical effects, including quantum interferences. These interferences have proved to be useful in several applications, including the detection of symmetric motifs in graphs via continuous-time quantum walks [8] and graph embedding by means of quantum commute times [9].

One difference between the approach in [7] and ours is that in the WKS, the time variable is not considered. In order to do so, the limiting average time behaviour (in the infinity) is computed. However, Rossi et al. [8] show that this choice is sub-optimal when used for measuring the similarity between two graphs. Alternatively, our approach relies on choosing proper finite limiting times. Our process is data driven (validated by the experiments) but herein we argue in favor of relating these limiting times with the *transport efficiency* of the quantum walk. Therefore, the long-term objective of this line of research is to choose the limiting times that *maximize transport efficiency*.

Another difference between WKS and our representation is that we do not compare the wave signatures between two nodes in the graph, but consider simultaneously all of them as forming a time-parameterized wave.

It must be stressed though that we do not claim that our method is in any sense a quantum algorithm. So we do not consider the issue of whether the characterization developed is observable or not. We are primarily interested in the complex nature of the characterization provided by the Schrödinger equation and the resulting non-stationarity and non-ergodicity of the dynamic system associated with it. Since the dynamic system is non-stationary and non-ergodic, it makes sense neither to characterize it using its steady state behaviour (since this does exist) nor its phase transitions (as is the case in the heat flow method). Instead we turn to the Fourier transform as a natural way of providing a frequency domain characterization of the time evolution of the complex wave equation, and use this instead of the heat flow trace [4].

The resulting representation relates frequency and graph structure by establishing a link between structural pattern analysis and diffraction theory. Diffraction theory is the basis of methods such as X-ray diffraction which allows molecular structure to be recovered from diffraction patterns. The seminal achievement here was the determination of the structure of DNA from Rosalind Franklin's skilfull diffraction imagery by Crick and Watson [12]. The diffraction pattern is a spatial pattern, and so it is an embedding of a graph on the 2D plane. The sym-

metry planes of the graph-structure are manifest as sets of geometrically regular frequency peaks. Thus we transform the characterzation of graph structure into a problem of searching for geometric regularity in a set of points.

In Section 2 we compare the Schrödinger operator with the heat kernel (both are governed by the eigensystem of the graph Laplacian). In Section 3 we analyze the operator and build a parametric representation from its spatio-temporal power spectrum. Such representation is transferred to a point in a suitable Stiefel manifold and principal angles are used for graph comparison. In Section 4 we show that the proposed approach outperforms state-of-the-art graph matching methods. Finally, in Section 5 we present our conclusions and future work.

## 2 Heat Kernel Vs. Schrödinger Operator

### 2.1 Heat Kernel

Let $G = (V, E)$ be an undirected graph where $V$ is its set of nodes and $E \subseteq V \times V$ is its set of edges. The Laplacian matrix $L = D - A$ is constructed from the $n \times n$ adjacency matrix $A$ with $n = |V|$, in which the element $A(u, v) = 1$ if $(u, v) \in E$ and 0 otherwise, where the elements of the diagonal $n \times n$ degree matrix are $D(u, u) = \sum_{v \in V} A(u, v)$. The $n \times n$ heat kernel matrix $K_t$ is the fundamental solution of the heat equation

$$\frac{\partial K_t}{\partial t} = -LK_t, \tag{1}$$

and depends on the Laplacian matrix $L$ and time $t$. The form of the heat kernel matrix is $K_t = e^{-Lt}$. The continuous time random walk starting at $p_0 \in \mathbb{R}^n$ evolves as $p_t = K_t p_0$, where $p_t$ is the state of the random walk at time $t$. The spectral decomposition of the Laplacian is $L = \Phi \Lambda \Phi^T$, where $\Phi = [\phi_1|\phi_2|\ldots|\phi_n]$ is the $n \times n$ matrix of ordered eigenvectors according to the corresponding eigenvalues $0 = \lambda_1 \leq \lambda_2 \leq \ldots \leq \lambda_n$, and $\Lambda = diag(\lambda_1\ \lambda_2\ \ldots\ \lambda_n)$. Therefore, the spectral decomposition of the heat kernel is $K_t = \Phi e^{-\Lambda t} \Phi^T$ where $e^{-\Lambda t} = diag(e^{-\lambda_1 t}\, e^{-\lambda_2 t}\ \ldots\ e^{-\lambda_n t})$, that is, the heat kernel and the Laplacian share their eigenfunctions, which are contained in $\Phi$. Both the columns and the rows of $\Phi$ define orthonormal basis: $\phi_i^T \phi_j = \delta_{ij}$.

### 2.2 Schrödinger Operator

The Schrödinger equation describes how the complex state vector $|\psi_t\rangle \in \mathbb{C}^n$ of a continuous-time quantum walk varies with time [10]:

$$\frac{\partial |\psi_t\rangle}{\partial t} = -iL|\psi_t\rangle. \tag{2}$$

Given an initial state $|\psi_0\rangle$ the latter equation can be solved to give $|\psi_t\rangle = \Psi_t|\psi_0\rangle$, where $\Psi_t = e^{-iLt}$ is a complex $n \times n$ *unitary matrix*. In this paper we refer to $\Psi_t$ as the *Schrödinger operator* and we focus our attention on the operator

itself and not on the quantum walk process. In this regard, Stone's theorem [13] establishes a one-to-one correspondence between a time parameterized unitary matrix $U_t$ and a self-adjoint (Hermitian) operator $H = H^*$ such that there is a unique Hermitian operator satisfying $U = e^{itH}$. Such an operator $H$ is the *Hamiltonian*. In the case of graphs we may set $H = -L$ and then we have that $\Psi_t = e^{-itL}$ is a unitary matrix for $t \in \mathbb{R}$.

Unitary matrices play a fundamental role in *characterizing complex wave equations* in a manner analogous to that performed by doubly stochastic matrices in characterizing diffusion processes. A $n \times n$ complex matrix $U$ is unitary if $U^\dagger U = UU^\dagger = I_n$, where $U^\dagger$ is the conjugate transpose, that is $(A^\dagger)_{ij} = \overline{A_{ji}}$. Therefore, both the rows and columns of $U$ form a orthonormal basis in $\mathbb{C}^n$. $U$ is diagonalizable via the factorization $U = V\Lambda V^\dagger$ where $\Lambda$ contains the complex eigenvalues of $U$ and $V$ is unitary and its columns contain the eigenvectors of $U$. Combining the latter diagonalization with the property $|det(U)| = 1$ we have that all the complex eigenvalues of $U$ must lie on the unit Argand circle. They must have either the form $e^{i\theta}$ or $e^{-i\theta}$ where $\theta$ is a rotation angle. More precisely, for $\Psi_t$ we obtain the spectral decomposition $\Psi_t = \Phi e^{-it\Lambda}\Phi^T$, where $\Phi$ contains the eigenvectors of $L$ and $e^{-i\Lambda t} = diag(e^{-i\lambda_1 t}\ e^{-i\lambda_2 t}\ \ldots\ e^{-i\lambda_n t}\ )$, the complex eigenvalues of $\Psi_t$, rely on the ones of the Laplacian.

Therefore, the Laplacian controls the dynamics of both the heat kernel and the Schrödinger operator according to the similarity between Eq. 2 and Eq. 1. However, this similarity is misleading since $\Psi_t$ is complex valued. The physical dynamics induced by the Schrödinger equation is therefore totally different from that of the heat equation, due to the existence of oscillations and interferences.

In this paper we address the question of whether the Schrödinger operator may be used to characterize the structure of a graph. Empirical analysis on different graph structures shows that both the heat kernel and the Schrödinger operator evolve with time in a manner which strongly depends on graph structure. [1] However, the underlying physics and the resulting dynamics are quite different (see Fig. 1 where for the heat kernel we represent $K_t(u, v)$ and for the Schrödinger operator we show the squared magnitude $|\Psi_t(u, v)|^2$). In the case of heat flow, heat diffuses between nodes through the edges, eventually creating transitive links (allowing effective energy exchange between nodes that are not directly connected by an edge), until reaching a stationary equilibrium state. The Schrödinger operator defines a wave which yields a faster energy propagation through the system (e.g. for a 100 nodes line graph, it takes $t = 50$ time steps for the Schrödinger operator to reach every possible position on the graph, taking more than twice this time in the case of the heat kernel [4]). Moreover, due to the negative components of the complex amplitudes, interferences are created, producing energy waves [5]. The main difference is that because of its wave nature the Schrödinger operator never reaches an equilibrium state. In other words, it is non-ergodic. Graph connectivity imposes constraints on the distribution of energy. In the case of the heat kernel, a larger number of en-

[1] Videos showing the evolution of both heat kernel and Schrödinger operator are available at `http://www.dccia.ua.es/~pablo/downloads/schrodinger_operator.zip`

ergy distribution constraints implies the creation of more transitive links with time [4]. This is true in the case of the Schrödinger operator, for which higher frequency and more symmetrical energy distribution patterns are also observed.

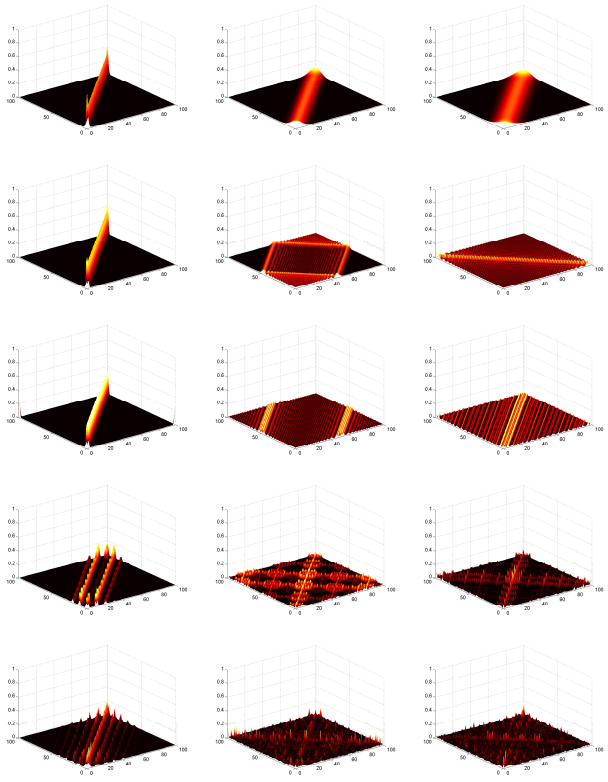

**Fig. 1.** Evolution with time ($t = 1, 25$ and 100). From top to bottom: heat kernel for a 100 node line graph, Schrödinger operator for a 100 node line graph, Schrödinger operator for a 100 node circle graph, Schrödinger operator for a 10×10 grid graph with 4 neighbour connectivity and Schrödinger operator for a 10×10 grid graph with 8 neighbour connectivity. (Courtesy of Pablo Suau)

## 3 Analysis of the Schrödinger Operator

### 3.1 Non-Ergodicity

In order to explore the ergodicity of the Schrödinger operator we consider both its spectral decomposition $\Psi_t = \Phi e^{-it\Lambda}\Phi^T$ and that of the heat kernel $K_t =$

$\Phi e^{-t\Lambda}\Phi^T$, that is

$$\Psi_t = \sum_{k=1}^{n} e^{-it\lambda_k}\phi_k\phi_k^T \text{ and } K_t = \sum_{k=1}^{n} e^{-t\lambda_k}\phi_k\phi_k^T, \tag{3}$$

where $\lambda_k$ is the k-th eigenvalue of the Laplacian $L$ and $\phi_k$ its corresponding eigenvector. Therefore, both operators are specified by the eigenfunctions of the Laplacian but in a very different way. The spectral decomposition of the heat kernel demonstrates that it is dominated by the lowest eigenvalues, due to the fact that $\lim_{t\to\infty} e^{-t\lambda_k} = 0$. However, the limit of $e^{-it\lambda_k} = \cos(t\lambda_k) - i\sin(t\lambda_k)$ when $t$ tends to infinity is undefined. Thus, there are two important differences with the heat kernel. Firstly, the Schrödinger operator never converges (it is non-ergodic), and secondly, it is not dominated by any particular eigenvalue. This is consistent with the well known physics of waves since the Schrödinger operator is a linear combination of waves.

### 3.2 Regimes Dynamics of Wave Propagation

The behavior of the Schrödinger operator at small and large times responds to different aspects of graph structure. At low $t$, the edge constraints contained in the Laplacian dominate (see left column in Fig. 1). At high $t$, on the other hand, it is the path structure that dominates (see the rest of the columns in Fig. 1).

In addition, the two regimes can be explained by the fact that the largest amplitudes occur at low frequencies. More precisely, each entry $\Psi_t(u,v)$ is described by a *linear combination of complex rotations*:

$$\Psi_t(u,v) = \begin{cases} \sum_{k=1}^{n} e^{-i\lambda_k t}\phi_k(u)\phi_k(v) & \text{if } u \neq v \\ \sum_{k=1}^{n} e^{-i\lambda_k t}\phi_k^2(u) & \text{otherwise .} \end{cases} \tag{4}$$

We let $z_k(u,v) = \phi_k(u)\phi_k(v)$ if $u \neq v$ and $z_k(u,v) = \phi_k(u)^2$ otherwise. In this case $z_k(u,v) \in \mathbb{R}$ for each value relies on the $k-$th eigenvector $\phi_k$ of the Laplacian. Since

$$|\Psi_t(u,v)|^2 = \sum_{k=1}^{n}\sum_{l=k}^{n} z_k(u,v)z_l(u,v)2\cos(t(\lambda_l - \lambda_k)) \tag{5}$$

we have that

$$\lim_{t\to 0}|\Psi_t(u,v)|^2 = 2\sum_{k=1}^{n}\sum_{l=k}^{n} z_k(u,v)z_l(u,v) \tag{6}$$

yields the maximal amplitude at $(u,v)$ since $z_k(u,v)$ and $z_l(u,v)$ are time independent. As $t$ increases the differences $\lambda_l - \lambda_k$, which are also time independent, become significant. They define lower or equal amplitudes and the characteristic frequency content of the wave emerges as expected. Low amplitudes dominate due to the ordering of the eigenvectors of the Laplacian $0 = \lambda_1 \leq \lambda_2 \leq \ldots \leq \lambda_n$ although there are always $n$ terms where $\lambda_l = \lambda_k$. The latter property (dominance) is preserved as much as the graph is connected.

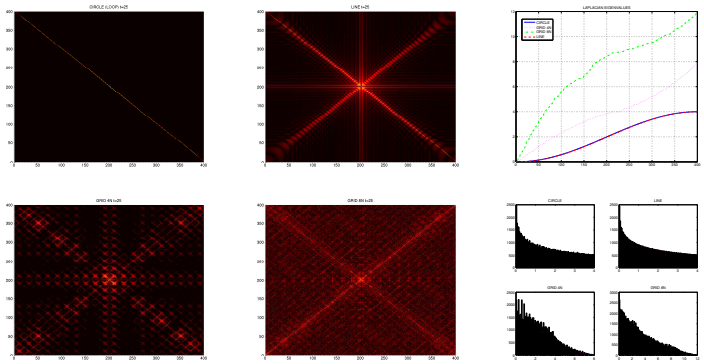

**Fig. 2.** Power spectra of the Schrödinger operator for different graphs of 400 nodes at $t = 25$: circle (loop) graph (top-left), line graph (top-middle), 20×20 grid graph with 4 neighbor connectivity (bottom-left) and 20×20 grid graph with 8 neighbor connectivity. For the latter graphs we also show their spectra (top-right) and the multiplicity of each value of $\Delta_{kl}$ (bottom-right).

### 3.3 Expressiveness of the Schrödinger Power Spectra

The discrete Fourier transform (DFT) of the squared magnitude of the Schrödinger Operator $\Psi_t$ is

$$\begin{aligned}\mathcal{F}_t(\omega_u,\omega_v) &= \sum_{u,v=1}^{n} |\Psi_t(u,v)|^2 e^{-i(\omega_u u+\omega_v v)} \\ &= \sum_{u,v=1}^{n} \left( \sum_{k=1,l=k}^{n} Z_{kl}\delta(t\Delta_{kl} - (\omega_u u+\omega_v v)) + \right. \\ &\quad \left. \sum_{k=1,l=k}^{n} Z_{kl}\delta(t\Delta_{kl} + (\omega_u u+\omega_v v)) \right), \end{aligned} \tag{7}$$

where $\omega_u$ and $\omega_v$ are the angular frequencies, $\Delta_{kl} = \lambda_l - \lambda_k \geq 0$, $Z_{kl} = z_k(u,v)z_l(u,v)$, and $\delta(.)$ is the Dirac delta function resulting from the Fourier transforms of $2\cos(t(\Delta_{kl})) = e^{it\Delta_{kl}} + e^{-it\Delta_{kl}}$ (see Eq. 5) for $k = 1,\ldots,n$, $l = k,\ldots,n$. After shifting we have that the amplitude $A_t(\omega_u,\omega_v) = |\mathcal{F}_t(\omega_u,\omega_v)|$ is given by pooling the values relying on $\sum_{k=1,l=k}^{n} Z_{kl}$ at all points $(u,v)$ belonging to the lines $t\Delta_{kl} = \omega_u u + \omega_v v$ ($t\Delta_{kl}$ gives the distance to the origin and the vector $[\omega_u,\omega_v]^T$ is perpendicular to the direction of the line). Therefore the energy (power) distribution is determined by both the spectrum of the Laplacian, which defines the gaps $\Delta_{kl}$, and its eigenvectors which define the values of $\sum_{k=1,l=k}^{n} Z_{kl}$.

In Fig. 2 we show the power spectra of the Schrödinger operators for scaled versions of the graphs analyzed in Fig. 1. These images resemble responses to

diffraction gratings (interference patterns). In diffraction theory, interference patterns emerge when waves are bent around edges or slits. Constructive and destructive interferences occur producing alternate bright and dark fringes (see for instance the Young's experiment) which fade away from the center. The distribution of the so called Bragg's peaks (associated to constructive interferences) relies both on wavelengths and the number and spacings between the slits, as well as it also depends on the incidence angle. Fringes become sharper, for instance, as the number of slits is increased but, in this case, they are characterized by less and less significant maxima of intensity. In X-ray crystallography, the interdependence between the spatial distribution (e.g. a lattice) of the atoms, the properties of incident light and diffraction patterns is exploited to infer the tridimensional density of electrons in a crystal as well as to solve the structure of organic molecules like proteins. When applying this ideas to characterize pure topological structures like graphs, we realized that the Schrödinger operator provides a natural way of encoding the latter interdependences: the complex exponentiation of the Hamiltonian (the negative Laplacian) produces a wave equation completely determined by the spectrum and eigenvectors of such Hamiltonian. In addition, there is a correspondence between interference patterns and Fourier transforms. Actually, the Fourier transform in Eq. 7 has the same form of an aperture used in Fraunhofer diffraction: $a[\delta(x-S/2)+\delta(x+S/2)]$ where $S$ is the distance between two slits. This gives us an interpretation of $A[\delta(t\Delta_{kl}-(\omega_u u+\omega_v v))+\delta(t\Delta_{kl}+(\omega_u u+\omega_v v))]$ where $A=\sum_{u,v=1}^{n}\sum_{k=1,l=k}^{n} Z_{kl}$ in terms of the topological constraints that must be satisfied in order to produce Bragg's peaks. In our case, the role of the slits is played by the spectra (more precisely by the gaps $\Delta_{kl}$) and the eigenvectors of the Laplacian. They determine what frequencies (energies in the power spectra) can be seen in the diffraction pattern. For instance, in circle (ring) graphs Fig. 2 (top-left) shows that the energy distribution may be constrained to lie at $0 = u + v$. For a line (path) graph (top-middle) we have a richer energy distribution although the line and circle graphs are quasi iso-spectral. Grid graphs are endowed with even richer diffraction patterns (larger range of eigenvalues).

The above rationale can be summarized as follows. Graphs produce diffraction patterns in the power spectra imposed by their Laplacians. This intuition is again borrowed from physics. Therefore, the analysis of the the Schrödinger operator can be posed in terms of analyzing its power spectra in order to explain the distribution of the different frequency amplitudes and their meaning. So far we have provided a geometric interpretation. In this regard, it is key to find the relation, if any, between the anisotropies in the power spectra and the lack of regularity in the structure. Such anisotropy is poorly contemplated in well known models of holistic image characterization [14],[15]. However, despite existing models in image characterization are not directly applicable to describe graph-based diffraction patterns, the underlying methodology (including PCA/SVD eigenspaces) can be extended to incorporate anisotropy. In order to do that we will exploit the spatio-temporal nature of the Schrödinger operator.

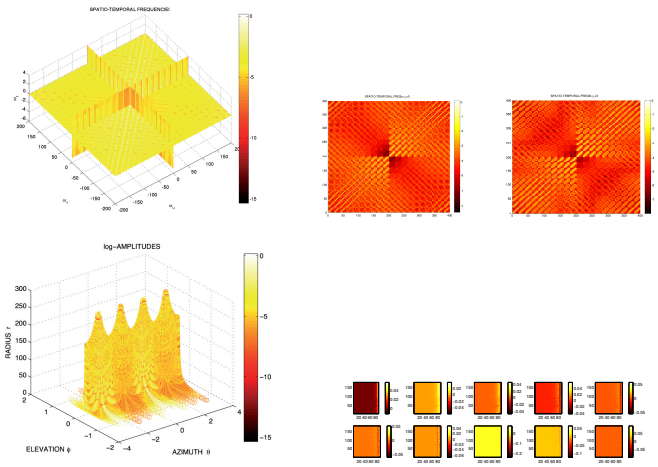


**Fig. 3.** Spatio-Temporal Power spectra of the Schrödinger operator for a 20×20 grid graph with 4 neighbor connectivity. Top-left: planes $\omega_u = 0$, $\omega_v = 0$, $\omega_{t'} = 0$. Top-center/right: detail of $\omega_{t'} = 0$ and $\omega_{t'} = 3$ showing parallel high pooled lines. Bottom-left: spherical coordinates of log-amplitudes. Bottom-right: 10 principal eigenvectors of the $\theta - \phi$ space.

### 3.4 Characterization of the Spatio-Temporal Schrödinger Power Spectra

Let $\mathcal{F}(\omega_u, \omega_v, \omega_t)$ be the spatio-temporal DFT of $|\Psi(u, v, t)|^2$. It is straightforward to extend Eq. 7 to include time variation. As expected, after shifting the transform we have that the amplitudes $A(\omega_u, \omega_v, \omega_t) = |f(\omega_u, \omega_v, \omega_t)|$ are given by pooling the values relying on $\sum_{k=1,l=k}^{n} Z_{kl}$ at all points $(u, v, t)$ belonging to the planes $t\Delta_{kl} = \omega_u u + \omega_v v + \omega_t t$. Furthermore, since the gaps $\Delta_{kl}$ are time independent, scaled temporal frequencies $\omega_t t$ can be seen as offsets in the spatial constraints $t\Delta_{kl} = \omega_u u + \omega_v v$. Such offsets are needed to explain the spatio-temporal behavior of the Schrödinger operator. More precisely, for $t > 0$ and $\omega_t \neq 0$ only the contributions $\sum_{k=1,l=k}^{n} Z_{kl}$ at $(u, v, t)$ where $(u, v)$ do not satisfy $t\Delta_{kl} = \omega_u u + \omega_v v$ are taken into account for computing the amplitudes $A(\omega_u, \omega_v, \omega_t)$.

An interesting particular case of the latter rationale is to pool amplitudes from $(u, v)$ satisfying constraints which are orthogonal to the spatial ones. For instance, in Fig. 3 (top-left) we show the spatio-temporal log-amplitudes for the planes $w_u = 0$, $w_v = 0$ and $w_{t'} = 0$ where $t' = t - T/2$ being $[0, T]$ the temporal interval of analysis. The graph analyzed is the $20 \times 20$ grid with 4 neighbors connectivity. In Fig. 3 (top-center/right) we show respectively the planes $\omega_{t'} = 0$ and $\omega_{t'} = 3$. Both of them are characterized by high log-amplitudes at lines $w_v = w_u \pm k$, with $k \geq 0$, which are orthogonal to those which have a similar degree of pooling at a particular $t'$ (see Fig. 2 (bottom-left)). The highest pooling is obtained at $k = 0$, that is $w_u = w_v$, and it decreases as $|k|$ in-

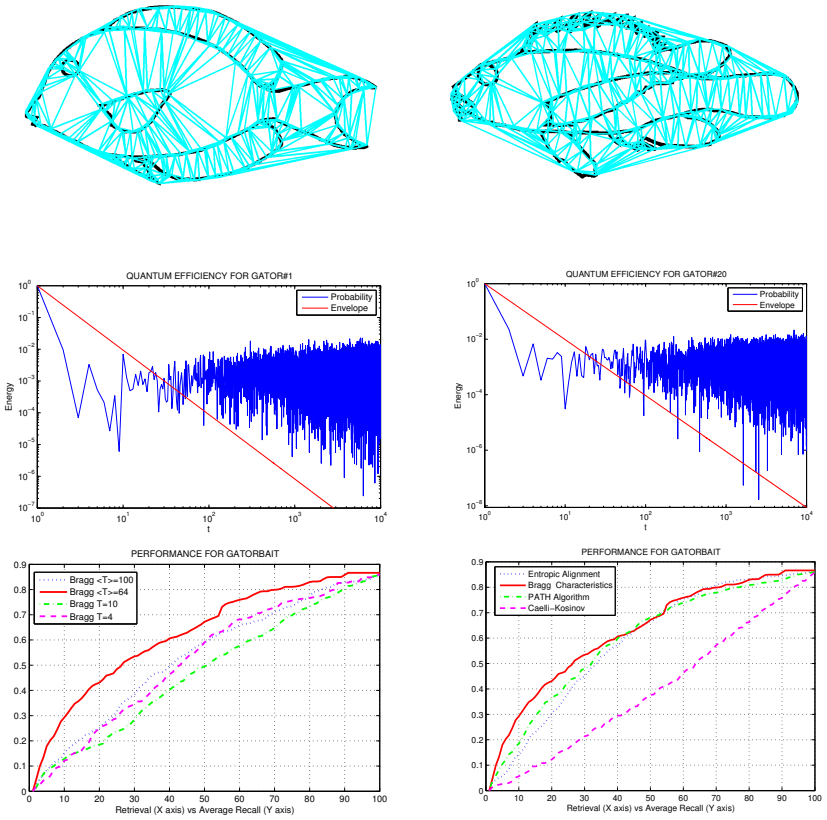


**Fig. 4.** Experimental Results. Top: Delaunay graphs of Gatorbait - Gator#1 (left) vs-Gator#20 (right). Middle: Quantum Efficiency for Gator#1 (left) vs QE for Gator#20 (right); The intercept for the first one is smaller almost one order of magnitude that that of the second. Bottom: Average Recall vs Retrieval curves. Best performance is achieved with $T = 64$ on average, even when larger values of $T$ are assumed (left). The result outperforms state-of-the-art graph matching algorithms (right). In all cases classes with only one element are not considered for measuring the performance.

creases. This happens for $sign(\omega_u) = sign(\omega_v)$. Otherwise we have the inverse case: log-amplitudes increase with $|k|$ (at $\omega_{t'} = 0$ such increase is more spatially constrained than at $\omega_{t'} = 3$).

Once the role of temporal frequencies is clarified, it is convenient to change the coordinate system in order to better visualize the angular asymmetries in the spatio-temporal domain (anisotropy). Given $(\omega_u, \omega_v, \omega_t)$ its spherical coordinates are given by $(r, \theta, \phi)$ where $r = \sqrt{\omega_u^2 + \omega_v^2 + \omega_t^2}$ is the radius, $\theta = \tan^{-1}(\frac{\omega_v}{\omega_u})$, $-\pi \leq \theta \leq \pi$ is the azimuthal angle in the $\omega_u - \omega_v$ plane and $\phi = \cos^{-1}(\frac{\omega_t}{r})$, $-\frac{\pi}{2} \leq \phi \leq \frac{\pi}{2}$ is the elevation angle. Therefore, $r$ encodes the magnitude of the spatio-temporal frequencies, $\theta$ refers to the relation between spatial frequencies and $\phi$ gives the relative importance of temporal frequencies. In addition, for a given pair $\alpha_s = (\theta, \phi)$ the power spectrum $A(\alpha_s)^2$ decays with $r$ and such decay does not follows, in general, a power law. In addition, for $\alpha_{s+\Delta} = (\theta + \Delta, \phi + \Delta)$, with $|\Delta| > 0$ as small as possible, we have that $A(\alpha_{s+\Delta})^2$ differs significantly from $A(\alpha_s)^2$ in the general case (directional anisotropy).

In Fig. 3 (bottom-left) we plot the $r - \theta - \phi$ space for the log-amplitudes. The representation is symmetric with respect to the elevation axis $\theta = 0$ and it is periodic with respect to the azimuthal axis $\phi = 0$. Therefore, for the sake of computational efficiency we can define a discrete $\theta - \phi$ *elevation-azimuth space* by setting: $\theta \in [0, \pi/2]$, $\phi \in [0, \pi]$. Such space relates spatial and temporal frequencies. In addition, for each discrete radius $r \in [0, r_{max}]$, where $r_{max} = n/2$, we define a *sample space* $X_r$ as the log-amplitudes $\log A(r, \alpha_s)$ at all coordinates of the $\theta - \phi$ parametric space. Performing SVD/PCA analysis on the set of sample spaces $\mathcal{S} = \{X_r\}$ the principal eigenvalues $\lambda_1 \geq \lambda_2 \geq \ldots \geq \lambda_p$ with $p \ll d$, where $d = \delta_\theta \times \delta_\phi$ is the number of cells, encode the degree of directional anisotropy. Their associated $d-$dimensional eigenvectors $u_1, u_2, \ldots, u_p$ define a subspace where we compress all the spatio-temporal information of the operator.

The latter representation allows us to map a graph to a multi-layered parametric space (one layer per radial samples). Then, such space is encoded by a set of eigenvectors as it is done when analyzing image sequences. In this regard, it becomes very useful to consider each set of eigenvectors (subspace) as a point in a given manifold in order to exploit the geodesics defined in it. The natural choice is to consider that $U = [u_1\ u_2\ \ldots\ u_p]$ is a point in the Stiefel manifold $St(p, d) = \{U \in \mathbb{R}^{d \times p} : U^T U = I_p\}$, that is, the set of $d \times p$ matrices with orthonormal columns [16]. In Fig. 3 (bottom-right) we show the first $p = 10$ eigenvectors which define the Stiefel point associated to the $20 \times 20$ 4N grid graph. Given the spatial structure of log-amplitudes in spherical coordinates, global details appear close to $\pi/2$ in the azimuthal axis whereas local details are highlighted at lower values.

Stiefel manifolds are endowed with a Riemannian mathematical structure and therefore it is more convenient to define dissimilarities beyond the Frobenius or Euclidean distances, that is, which account for the curvature of the manifold where these subspaces lie [19] [20]. One of these dissimilarities relies on the concept of principal angle [17][18]. Given two points $U$ and $V$ in $St(p, d)$, the principal angles $0 \leq \theta_1 \leq \theta_2 \leq \ldots \leq \theta_p \leq \pi/2$ between the subspaces $Span(U)$

and $Span(V)$ satisfy that $\cos(\theta_i)$ are the singular values of $U^T V$ and the geodesic distance between $U$ and $V$ is given by $||\Theta||$ where $\Theta = [\theta_1 \theta_2 \dots \theta_p]$. In this paper, given two graphs $G_X = (V_X, E_X)$ and $G_Y = (V_Y, E_V)$ and the Stiefel points $U_X$ and $U_Y$ derived from the corresponding spatio-temporal Schrödinger power spectra, we will quantify the dissimilarity between the two graphs in terms of the principal angles.

## 4 Experiments

### 4.1 GatorBait Database and Quantum Efficiency

In order to test our graph characterization method we use the *GatorBait_100* ichthyology database. GatorBait has 100 shapes representing fishes from 30 different classes. Shapes are discretized and then Delaunay triangulation graphs (included in the publicly accessible UA Graph Database[2] ) are retained for testing graph comparison/matching algorithms [21].

Gaps distribution is very important since it is known that the transport efficiency of quantum walks relies on it [23]. More precisely,

$$|\bar{\alpha}(t)|^2 = |(1/n)\sum_{k=1}^{n} e^{-it\lambda_k}|^2$$

is the probability that a continuous-time quantum walk returns to the origin at $t$. Such quantity is usually characterized by two regimes: for low-mid values of $t$ it decreases; at higher values, quantum oscillations around the long-term average dominate. This happens if the probability density function over the $\Delta_{kn}$ (the larger gaps) follows a power-law distribution, which is a mild assumption for Delaunay graphs. If so, the temporal range where quantum oscillations vanish is bounded by the intercept of $t^{-2(1+\nu)}$ (the so called *envelope* of the process) where $\nu$ is the power exponent. The smaller the intercept the higher the efficiency. This allows us to set the optimal value for $T$ within the range of the envelope. The intercept for each graph induces a partial order that can be used for scaling $T$ (see Fig. 4 (top) where vertical axes are fixed according to the minimal values of $|\bar{\alpha}(t)|^2$). It also explains why too-low or too-high uniform values of $T$ produce less discriminative characterizations that setting $T = 64$ *on average* (Fig. 4 (bottom-left)).

### 4.2 Comparison with Graph Matching Algorithms

In Fig. 4 we compare the discriminability of or characterization with state-of-the-art graph matching algorithm like Entropic Manifold Alignment [21][22] (which outperforms many others), the PATH algorithm [24] and the Caelli-Kosinov spectral algorithm [25], not evaluated in previous experiments. Their cost functions or associated kernels are used for estimating similarity after alignment. In

[2] http://www.rvg.ua.es/graphs/dataset01.html

Fig. 4 (bottom-right) we show that our approach (setting $T = 64$ on average) outperforms the alternatives in terms of average recall in the part of the curve where the number of retrievals is small or medium. Only when a high number of retrievals is allowed (usually avoided in practice) the alternatives slightly improve our characterization.

## 5 Conclusion

In this paper we have proposed the use of Bragg diffraction patterns to characterize graphs. The representation of the spatio-temporal Fourier transform of the Schrödinger operator in terms of a Stiefel points produces high discrimination rates provided that quantum efficiency is considered. Future works include the formulation of finding the optimal $T$ that maximizes quantum transport efficiency.

**Acknowledgements** F. Escolano is funded by the project TIN2015-69077-P of the Spanish Government.

## References

1. Aziz, F., Wilson, R., Hancock, E.: Graph Characterization via Backtrackless Paths, Similarity-Based Pattern Recognition - First International Workshop, SIMBAD 2011, 2011
2. Peng, R., Wilson, R., Hancock, E.: Graph Characterization via Ihara Coefficients, IEEE Transactions on Neural Networks, 22(2), 233–245, 2011
3. Das, K. C.: Extremal Graph Characterization from the Bounds of the Spectral Radius of Weighted Graphs, Applied Mathematics and Computation, 217(18), 7420–7426, 2011
4. Escolano, F., Hancock, E., Lozano, M. A.: Heat Diffusion: Thermodynamic Depth Complexity of Networks, Physical Review E 85(3), 036206(15), 2012
5. Rossi, L., Torsello, A., Hancock, E.R, Wilson, R.C.: Characterizing Graph Symmetries through Quantum Jensen-Shannon Divergence, Physical Review E 88(3), 032806(9), 2013
6. Xiao, B., Hancock, E., Wilson, R.: Graph Characteristics from the Heat Kernel Trace, Pattern Reognition 42(11), 2589–2606, 2009
7. Aubry M., Schlickewei, U., Cremers, D.: The Wave Kernel Signature: A Quantum Mechanical Approach To Shape Analysis, IEEE International Conference on Computer Vision (ICCV), Workshop on Dynamic Shape Capture and Analysis (4DMOD), 2011
8. Rossi, L., Torsello, A., Hancock, E.: Approximate Axial Symmetries from Continuous Time Quantum Walks, Joint IAPR International Workshops on Structural and Syntactic Pattern Recognition and Statistical Techniques in Pattern Recognition (SSPR/SPR), 144–152, 2012
9. Emms, D., Wilson, R., Hancock, E.: Graph Embedding Using Quantum Commute Times, 6th IAPR-TC-15 International Workshop on Graph-Based Representations in Pattern Recognition (GBR), 371–382, 2007

10. Farhi, E., Gutmann, S.: Quantum Computation and Decision Trees, Physical Review A 58, 915–928, 1998
11. Sun, J., Ovsjanikov, M., Guibas, L.J.: A Concise and Provably Informative Multi-Scale Signature Based on Heat Diffusion, Comput. Graph. Forum 28(5): 1383–1392, 2009
12. Watson, J.D., Crick F.H.C.: A Structure for Deoxyribose Nucleic Acid. Nature 171 (4356): 737738. 1953
13. Stone, M.H.: On one-parameter Unitary Groups in Hilbert Space. Annals of Mathematics 33(3), 643–648, 1932
14. Oliva, A., Torralba A.: Modeling the Shape of a Scene: A Holistic Representation of the Spatial Envelope. Int. Journal of Computer Vision 42(3): 145–175, 2001
15. Torralba A., Oliva A.: Statistics of Natural Image Categories. Network 14: 391–412, 2003
16. Edelman, A., Arias, T. A., Smith, S. T.: The Geometry of Algorithms with Orthogonality Constraints. SIAM Journal Matrix Analysis and Application, 20(2):303353, 1999.
17. Kim,T.-K., Kittler, J., Cipolla, R.: Discriminative Learning and Recognition of Image Set Classes Using Canonical Correlations. IEEE Trans. Pattern Anal. Mach. Intell. 29(6): 1005-1018, 2007
18. Absil, P.-A., Mahony, R., Sepulchre,R: Optimization Algorithms on Matrix Manifolds. Princeton University Press, Princeton, NJ, USA, 2008
19. Turaga, P.K.,Veeraraghavan, A., Srivastava, A., Chellappa, R.: Statistical Computations on Grassmann and Stiefel Manifolds for Image and Video-Based Recognition. IEEE Trans. Pattern Anal. Mach. Intell. 33(11): 2273-2286, 2011
20. Harandi, M.T., Sanderson, C., Shirazi, S.A., Lovell, B.C.: Graph Embedding Discriminant Analysis on Grassmannian Manifolds for Improved Image Set Matching. CVPR 2011: 2705-2712, 2011
21. Escolano, F., Hancock, E.R., Lozano, M.A.: Graph matching through entropic manifold alignment. CVPR 2011: 2417-2424, 2011
22. Escolano, F., Hancock, E.R., Lozano, M.A.: Graph Similarity through Entropic Manifold Alignment. SIAM J. Imaging Sciences 10(2): 942-978 (2017)
23. Mülken, O., Blumen, A.: Continuous-time Quantum Walks: Models for Coherent Transport on Complex Networks. Physics Reports 502(23): 3787, 2011
24. Zaslavskiy, M., Bach, F., Vert, J.-P: A Path Following Algorithm for the Graph Matching Problem. IEEE Trans. on PAMI, 31(12):2227-2242, 2009
25. Caelli, T., Kosinov, S.: An Eigenspace Projection Clustering Method for Inexact Graph Matching. IEEE Trans. on PAMI, 26(4), 2004